# The Role of Photon Scattering in Optical Signal Distortion during Arrhythmia and Defibrillation

Martin J. Bishop,* Blanca Rodriguez,* Fujian Qu,† Igor R. Efimov,† David J. Gavaghan,* and Natalia A. Trayanova‡

*Oxford University Computing Laboratory, Oxford OX1 3QD, United Kingdom; †Department of Biomedical Engineering, Washington University, St. Louis, Missouri; and ‡Department of Biomedical Engineering, The Johns Hopkins University, Baltimore, Maryland

ABSTRACT Optical mapping of arrhythmias and defibrillation provides important insights; however, a limitation of the technique is signal distortion due to photon scattering. The goal of this experimental/simulation study is to investigate the role of three-dimensional photon scattering in optical signal distortion during ventricular tachycardia (VT) and defibrillation. A three-dimensional realistic bidomain rabbit ventricular model was combined with a model of photon transport. Shocks were applied via external electrodes to induce sustained VT, and transmembrane potentials ($V_m$) were compared with synthesized optical signals ($V_{opt}$). Fluorescent recordings were conducted in isolated rabbit hearts to validate simulation results. Results demonstrate that shock-induced membrane polarization magnitude is smaller in $V_{opt}$ and in experimental signals as compared to $V_m$. This is due to transduction of potentials from weakly polarized midmyocardium to the epicardium. During shock-induced reentry and in sustained VT, photon scattering, combined with complex wavefront dynamics, results in optical action potentials near a filament exhibiting i), elevated resting potential, ii), reduced amplitude relative to pacing, and iii), dual-humped morphologies. A shift of up to 4 mm in the phase singularity location was observed in $V_{opt}$ maps when compared to $V_m$. This combined experimental/simulation study provides an interpretation of optical recordings during VT and defibrillation.

## INTRODUCTION

Optical mapping is a powerful tool capable of providing high-resolution recordings of wavefront dynamics during arrhythmia and defibrillation. The technique has, however, an important limitation: signal distortion due to scattering of fluorescent photons from a three-dimensional (3D) volume of tissue beneath the recording site (1–5). It is thus unclear which characteristics of the recorded signal are due to underlying electrophysiological properties of the tissue and which are scattering artifact, leading to difficulties in experimental data interpretation.

A consequence of fluorescent scattering is that information regarding transmembrane potentials within the midmyocardium is transduced through the ventricular wall by scattered photons and is manifested in the optical signal. The scattering volume associated with a particular epicardial optical recording site represents the 3D region of tissue beneath the site from which the majority of detected fluorescent photons originate. Ding et al. (2) used Monte Carlo simulations of photon movement during optical mapping to show that 90% of photons recorded by a particular epicardial recording site originate from a tissue volume, approximately hemispherical in shape, which extends ~1–2 mm both radially and from depth, with the specific dimensions depending sensitively upon the particular dye and wavelength used.

Simulation studies using simplified geometries (1,3,4,6), and more recently a realistic ventricular model (5), have been conducted to provide insight into the distortion effects of this averaging of transmembrane potential levels from within the scattering volume upon the optical signals during pacing. These studies have explained characteristics of the paced optical signals that render them different from microelectrode recordings, such as prolonged action potential (AP) upstroke, and increased wavefront width (1,7). However, 3D photon-scattering distortions in fluorescent signals during events of complex spatiotemporal dynamics, such as arrhythmogenesis, have not yet been fully assessed (3).

Photon-scattering distortions in optical recordings have been suggested to underlie unusual characteristics of fluorescent signals, which, during arrhythmias, are at odds with microelectrode recordings, and in the case of defibrillation when electrical recordings during and shortly after the shock are not possible, at odds with realistic computer simulations. For instance, during sustained ventricular tachycardia (VT), photon scattering from the passage of a subsurface wavefront has been suggested to underlie the formation of dual-hump APs (3,8,9), which have never been documented in microelectrode recordings. Furthermore, the source of resting potential elevation and AP amplitude reduction observed in optical signals near the reentrant core remains a puzzle. Such phenomena cannot be explained by ion accumulation close to the core, as accumulations build up over a number of reentrant cycles (10).

Finally, there exists a disparity in the magnitude of the optically recorded and simulated virtual electrode polarization (VEP) induced by a defibrillation-strength shock (11).

*Submitted April 23, 2007, and accepted for publication July 12, 2007.*

Address reprint requests to Martin J. Bishop, Oxford University Computing Laboratory, Oxford OX1 3QD, UK. Tel.: 44-1865-283568; E-mail: martin.bishop@comlab.ox.ac.uk.

Editor: David W. Piston.



0006-3495/07/11/3714/13 $2.00

doi: 10.1529/biophysj.107.110981

Nonlinearity in the response of membrane-bound dyes at high transmembrane potentials has been deemed insufficient to account for such disparity (12). Instead, the difference has been attributed to the averaging effects of photon scattering (6,12). However, controversy remains over the specific depth from which optical signals arise (12). Detection of VEP within the depth of the ventricular wall is potentially important for studies of shock-induced arrhythmogenesis, in which knowledge of the location and extent of regions of intramural excitable gap is of vital importance to understanding shock outcome (11).

The goal of this study is to investigate the role of 3D photon scattering in signal distortion during optical recordings of arrhythmias and defibrillation. Specifically, we hypothesize that dual-hump APs, occurring near the reentrant core, can be directly attributed to 3D photon scattering but occur from a variety of specific mechanisms in which local ventricular geometry also plays a role. Further, we surmise that resting potential elevation/reduced AP amplitude of the optical signal near the reentrant core stem from photon scattering but are also consequences of complex wavefront propagation combined with optical mapping normalization techniques. Finally, we aim to demonstrate that the disparity between the magnitude of the optically recorded shock-end VEP and that predicted by realistic simulations of defibrillation is due to scattering of photons, which originate from midmyocardial regions of significantly weaker VEP relative to the epicardium.

To achieve our objectives, a 3D anatomically realistic bidomain model of the rabbit ventricles, which can represent at once VEP and origin of arrhythmias after defibrillation shocks, as well as sustained VT, is combined with a photon diffusion model accounting for illumination and fluorescent emission to simulate the synthesis of optical signals recorded by a panoramic mapping system. By comparing simulated transmembrane potential maps with simulated fluorescent maps on the ventricular surfaces, the mechanisms responsible for optical signal distortion can be effectively elucidated. To provide input regarding the optical parameters of rabbit ventricular tissue and to validate the optical simulation results, optical mapping experiments were conducted in isolated rabbit hearts.

## MATERIALS AND METHODS

### Experimental preparation

Excised hearts of young New Zealand white rabbits were placed on a Langendorff apparatus and perfused with oxygenated modified Tyrode's solution. Hearts were stained with the voltage-sensitive dye di-4-ANEPPS (Molecular Probes Eugene, OR). Excitation-contraction uncoupler 2,3-butanedione monoxime (BDM, Fisher Scientific, Fair Lawn, NJ) reduced motion artifacts. Hearts were positioned in a perfusion chamber (Fig. 1 *A*), and activity on the anterior was recorded optically, as described previously (8,9).

Measurement of light attenuation within ventricular tissue at illumination (545 ± 20 nm) and emission (610 ± 20 nm) wavelengths was performed in a manner similar to Baxter et al. (1). Briefly, a camera, aimed perpendicularly at the cut piece of tissue, shown in Fig. 2 *A* (*top*), recorded light attenuation with depth from the irradiated epicardium. Fig. 2 *A* (*bottom*) shows the field of view of the camera with respect to the preparation. Light intensities for each column in the field of view in Fig. 2 *A* (*bottom*) were summed. Single exponential decay functions were fitted to the data, and decay constants, representing penetration depths at the given wavelength, were determined as shown in Fig. 2 *B* for illumination (*top*) and emission (*bottom*). A monoexponential decay function was chosen as it has previously been shown to accurately model the decay of light intensity with depth in cardiac tissue (4). Exponential functions were only fitted to data points taken from depths >1 mm to account for misalignment of the nonplanar epicardial surface with the recording array. Optical penetration depths of 0.90 mm at the illumination wavelength and 2.10 mm at the emission wavelength were found, which agree well with values recorded at similar wavelengths in previous studies (1,2,4).

### Computational model

The anatomically based finite-element model of rabbit ventricles (Fig. 1 *B*) described previously (13) was used to simulate both electrical activation and photon scattering/absorption during illumination and emission. The model incorporated realistic geometry and fiber orientation and representations of the perfusing bath and the blood in the ventricular cavities. The distribution of transmembrane potential ($V_m$) throughout the ventricles was calculated using the bidomain equations. Membrane kinetics was represented by an augmented version of the Luo-Rudy dynamic model (14).

As in our previous publication (5), distribution of photon density after uniform epicardial illumination ($\Phi_{illum}$) was calculated throughout the ventricles using the steady-state photon diffusion equation and convoluted with the local value of $V_m$ to represent fluorescent emission intensity. The photon diffusion equation was again solved to calculate photon density at the emission wavelength ($\Phi_{em}$). Fick's law was used to relate the gradient of $\Phi_{em}$ at the epicardial surface to the photon flux recorded by the detector ($V_{opt}$). Optical signals were thus synthesized solely on the epicardial surface. Tissue optical properties at illumination and emission wavelengths were represented by penetration depths of 0.90 mm and 2.10 mm, respectively, as

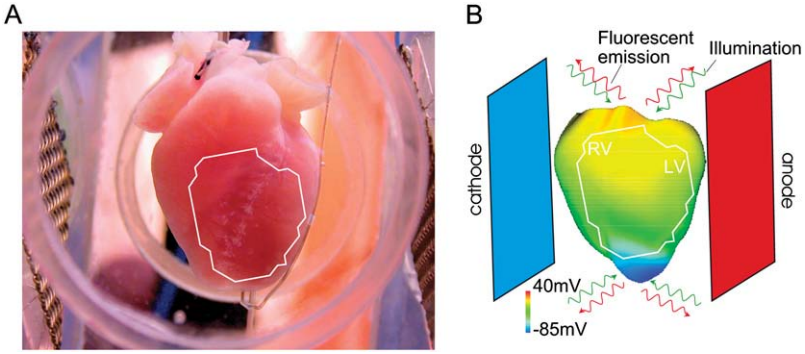


FIGURE 1 Langendorff-perfused rabbit heart (*A*) and rabbit ventricular model (*B*) with shock electrodes in perfusing chamber. The white outline represents the approximate optical system field of view. *B* presents preshock epicardial transmembrane potential distribution (CI = 140 ms).

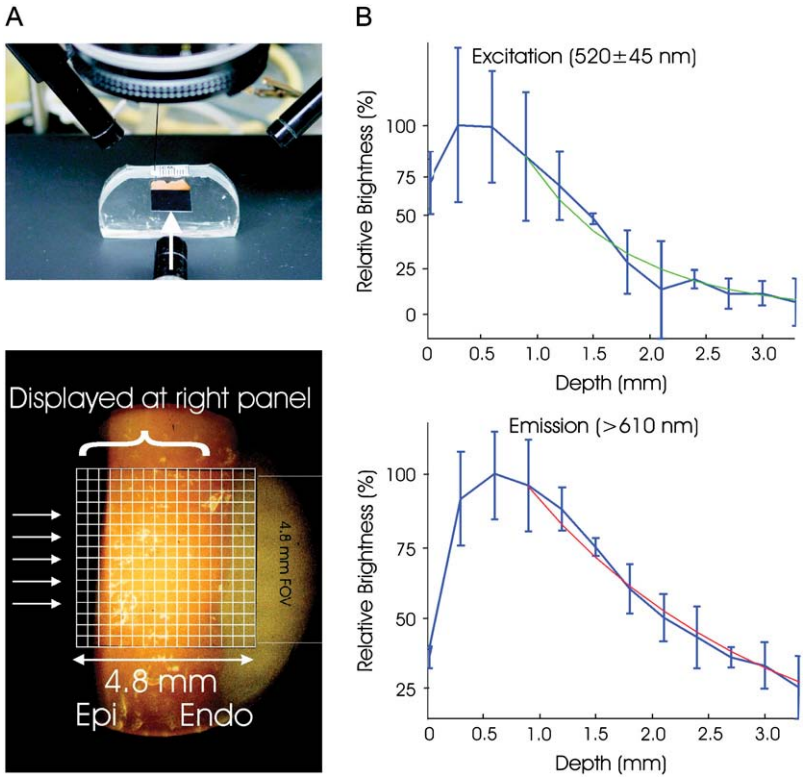


FIGURE 2 (*A*) Experimental setup used for determining optical penetration depths, showing the camera aimed perpendicularly at the cut tissue surface (*top*) and the grid for recording fluorescence intensity (*bottom*). (*B*) Summed light intensities (brightness) from each column in the recording grid plotted against depth into the tissue, shown in blue, with the corresponding single exponential fits for excitation illumination (*green curve*, *top*) and emission (*red curve*, *bottom*) wavelengths from which the respective optical penetration depths after excitation illumination and emission were determined.

measured in the experiments described above. Reflecting experimental uncertainty in optical penetration depth and the large variation between different preparations (2), additional simulations were performed in which penetration depths at both the illumination and emission wavelengths were varied simultaneously by between 0.5 and 1.5 times their default values. Thus, the effect of optical parameter uncertainty on simulated optical maps was assessed. Performing such an assessment is important, as changes in scattering/absorption properties of the tissue affect the penetration depths at illumination and emission as well as the scattering volume dimensions associated with a recording site, which correspondingly alter the amount of information contained in the fluorescent signal regarding the transmembrane potential distribution beneath the recording site. To aid comparison, $V_m$, $V_{opt}$, and $V_{exp}$ were normalized at each recording site using maximum/minimum AP values for that site after pacing, as in experimental recordings (8).

## Stimulation protocol

In simulations and experiments, a stimulus of twice the threshold and 4 ms duration was applied at 250 ms basic cycle length through a pacing electrode at the apex. After the eighth pacing stimulus, 8-ms-long truncated exponential monophasic shocks of varying shock strength (SS) were applied at a range of coupling intervals (CI) via mesh electrodes located at the vertical boundaries of the perfusing chamber (Fig. 1, *A* and *B*) (11). The cathode was located near the right ventricle (RV) and the anode near the left ventricle (LV). SS and CI were chosen such that shocks always resulted in sustained VT. This allowed us to generate $V_m$ maps at shock-end during shock-induced arrhythmogenesis (formation of reentry under conditions of residual VEP) and during sustained VT to be compared with the corresponding optical maps, synthesized or recorded experimentally as described above. Positions of scroll-wave filaments, the organizing centers of reentry, and corresponding phase singularities on the epicardial surface were determined as in Larson et al. (15) after prior computation of phase maps.

# RESULTS

## Recordings of shock-end VEP

Fig. 3 presents shock-end anterior epicardial VEP maps of transmembrane potential ($V_m$, *left*), synthesized optical ($V_{opt}$, *center*), and experimental ($V_{exp}$, *right*) signals for four combinations of SS/CI. For comparison between simulations and experiments, the white outline over simulated epicardial maps shows the optical field of view in the experiments. In the $V_m$ and $V_{opt}$ panels, we show two renderings of the data on the epicardium: in the left-hand maps, limits of the color scheme are 0 and 1 (normalized limits of the paced AP); in the right-hand map, limits are extended to $-0.2$ and 1.2. Since $V_m$ is calculated in the ventricular volume whereas $V_{opt}$ and $V_{exp}$ are only epicardial signals, Fig. 3 displays additional $V_m$ distributions in transverse and apex-to-base cross sections through the ventricles.

In both simulations and experiments, the shock induces areas of opposite-in-sign VEP on the epicardium (Fig. 3), consistent with previous findings (8,9,11). The LV surface near the anode is negatively polarized, whereas the RV surface is positively polarized with a region of intermediately polarized epicardium in between. In contrast, polarization within the ventricular wall is complex and exhibits a change in VEP sign between epi- and endocardium with the mid-myocardial wall experiencing weaker polarization than the surfaces.

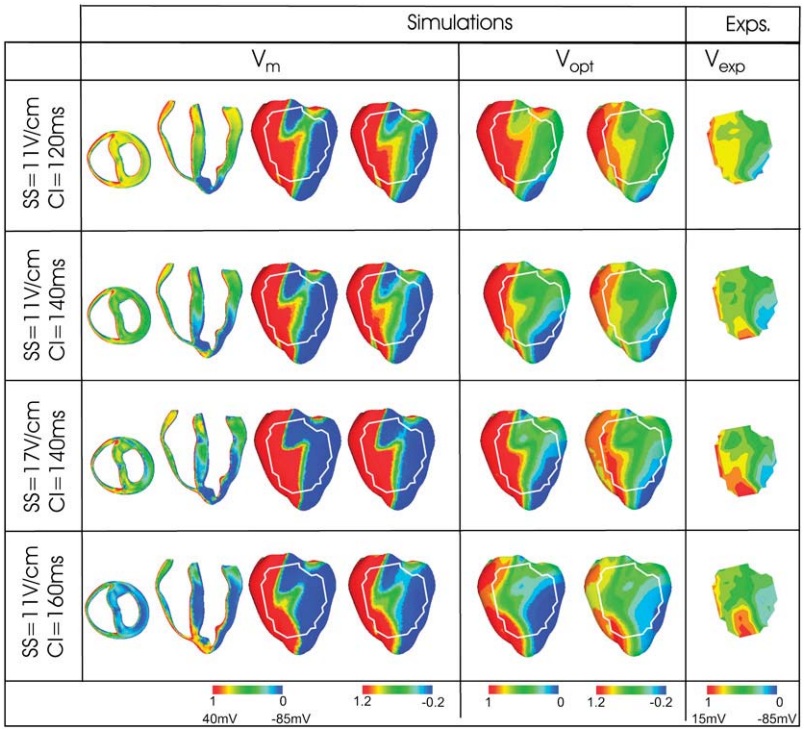


FIGURE 3 Shock-end VEP maps from simulations (*left*) and experiments (*right*) for various SS/CI combinations. Simulated maps include distributions of transmembrane potential ($V_m$, *left*) and optical signals ($V_{opt}$, *center*). Experimental maps, $V_{exp}$, are normalized between −85 and 15 mV. $V_m$ and $V_{opt}$ maps are presented with color scale limits between 0 and 1 (normalized limits of paced AP) (*left*) and between −0.2 and 1.2 (*right*). All optical maps show anterior epicardium, and $V_m$ distributions are also presented in transmural and apex-to-base cross sections. The white outline in the simulated maps shows experimental optical field of view.

Fig. 3 shows that photon scattering results in differences between $V_m$ and $V_{opt}$ maps, with $V_{opt}$ maps being a significantly better match to $V_{exp}$ maps than $V_m$ maps. Although in the $V_m$ maps the majority of the epicardium has strong positive/negative VEP, both $V_{opt}$ and $V_{exp}$ maps contain large areas of intermediate polarization. This finding is quantified in Fig. 4 *A*, which presents the percentage of epicardial area within the experimental field of view experiencing normalized polarization of $>0.7$, $0.3-0.7$, and $<0.3$. The percentage of intermediately polarized epicardium ($0.3-0.7$) in $V_{opt}$ maps is 44.1%, 55.8%, 40.0%, and 32.2% for the four cases in Fig. 3 (*top* to *bottom*); these are in close agreement with $V_{exp}$ values of 34.3% ± 12.1%, 49.0% ± 10.7%, 54.1% ± 6.3%, and 53.5% ± 15.8%. In contrast, $V_m$ maps show consistently smaller percentages of intermediately polarized epicardium, namely 20.1%, 15.9%, 7.2%, and 15.4% for the four cases in Fig. 3 (*top* to *bottom*).

Fig. 3 shows that photon scattering results in information on transmural VEP, visible in the transmural $V_m$ cross sections, being transduced through the myocardial wall and manifested in the surface $V_{opt}$ recordings. In the transmural $V_m$ VEP cross sections, for each SS/CI episode, large regions of the LV midmyocardial wall are negatively polarized (*dark blue*); these regions increase with the increase in CI. Direct comparison of these transmural $V_m$ maps with the corresponding epicardial $V_{opt}$ maps shows a consistent spatial alignment of the intramural excitable regions in the midmyocardium and areas of strong negative epicardial polarization in the $V_{opt}$ maps. To confirm that this effect is due to transduction, from depth, of information regarding polarization levels, $V_m$ images were replotted, scaled to the maximum and minimum $V_{opt}$ values (results not shown). The resulting pattern of VEP did not resemble the $V_{opt}$ VEP pattern (for example, there was no strong polarization close to the LV apex, above the intramural excitable gap), indicating that $V_m$ signals from deeper layers are contributing significantly to the $V_{opt}$ signal. Photon scattering also leads to a reduction in the range of VEP magnitude in $V_{opt}$ maps compared to $V_m$ maps; the match between simulated and experimental optical VEP maps indicates that the same distortion takes place in $V_{exp}$ signals.

Fig. 4 *B* shows the maximum and minimum values of normalized VEP, within the experimental field of view on the epicardium, for the $V_m$, $V_{opt}$, and $V_{exp}$ maps shown in Fig. 3. $V_m$ and $V_{exp}$ polarization ranges differ by up to 103% for all episodes of 11 V/cm strength (three different CIs) and up to 170% for the SS = 17V/cm and CI = 140 ms case. This difference is significantly reduced when photon scattering is taken into account: the difference between $V_{opt}$ and $V_{exp}$ ranges of VEP magnitude is $<20\%$ for the three cases of SS = 11 V/cm shown in the figure and $<31\%$ for the SS = 17 V/cm case. Therefore, in the VEP images of Fig. 3, if we adjust the normalization limits by just 20% from 0–1 to −0.2–1.2, we obtain an improved qualitative VEP pattern match between $V_{opt}$ and $V_{exp}$ maps (*right image* in each panel of Fig. 3).

We have recently shown that variations in tissue scattering/absorption properties can affect the level of distortion

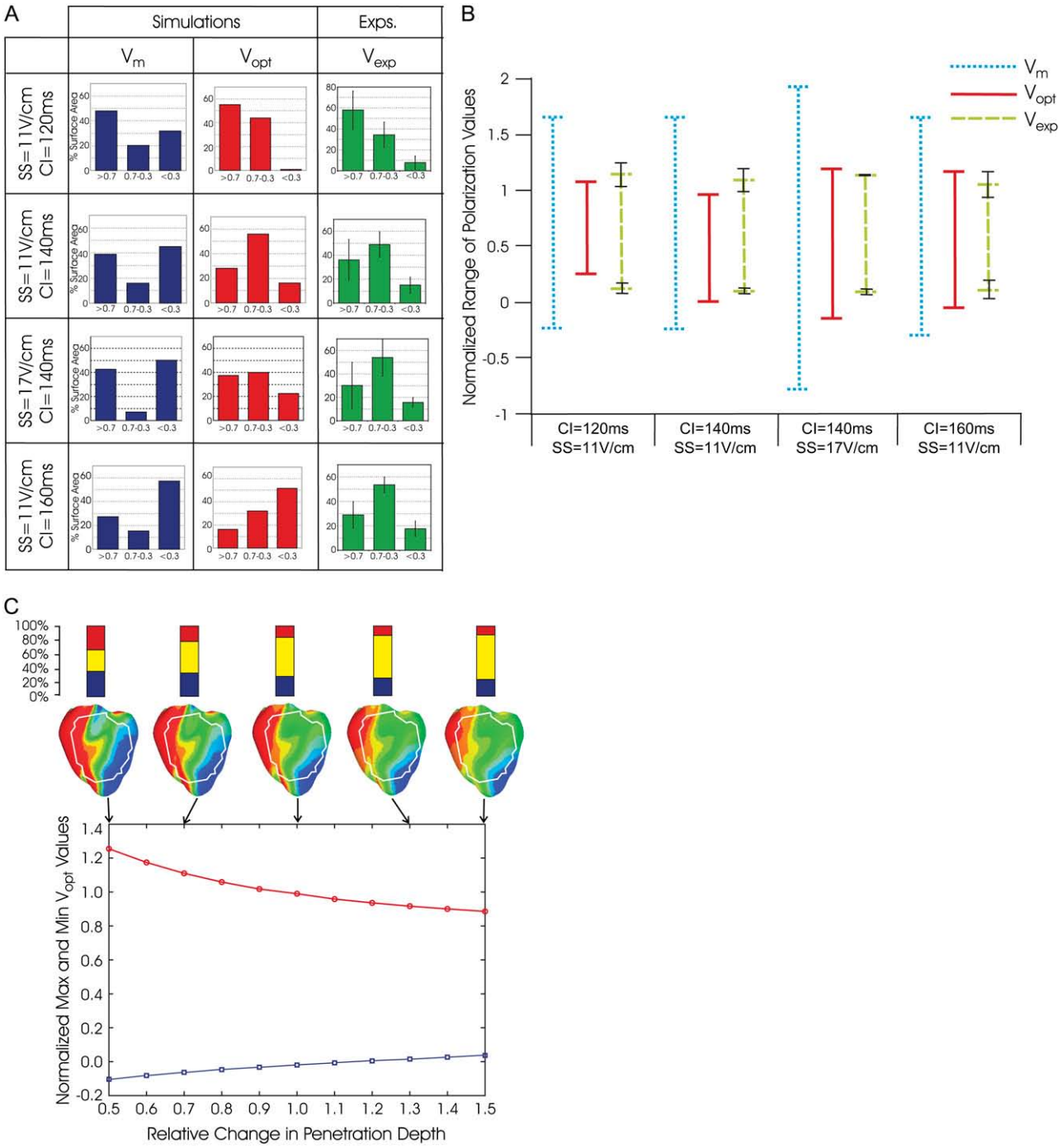


FIGURE 4 (*A*) Percentage of surface area, within experimental field of view, of polarization values >0.7, 0.3–0.7, and <0.3, for $V_m$, $V_{opt}$, and $V_{exp}$ maps and for different combinations of SS/CI. For $V_{exp}$, mean values are shown with error bars of one standard deviation. For each SS/CI, the number of rabbits in experiments varied as follows: $n = 4$ (11 V/cm/120 ms); $n = 5$ (11 V/cm/140 ms); and $n = 2$ (17 V/cm/140 ms); and $n = 5$ (11 V/cm/160 ms). (*B*) Range of normalized polarization values in $V_m$, $V_{opt}$, and $V_{exp}$ within experimental field of view for episodes shown in Fig. 3 *A*. (*C*) Variation in maximum/minimum normalized $V_{opt}$ polarization shown in *B* for the CI = 140 ms/SS = 11 V/cm episode as penetration depths at illumination and emission wavelengths change simultaneously by relative fractions between 0.5 and 1.5. Corresponding $V_{opt}$ polarization distributions are shown for selected penetration depths, along with representations of percentage of area within the experimental field of view having normalized VEP of >0.7, 0.3–0.7, and <0.3.

in optical AP upstroke during pacing (5). In Fig. 4 *C*, we present variations in maximum and minimum VEP for the SS = 11 V/cm/CI = 140 ms case (Fig. 3) as penetration depths during illumination and emission are simultaneously varied. $V_{opt}$ maps of VEP for specific penetration depths (indicated by *arrows*) are also shown along with corresponding representations of the percentage of positively (>0.7), negatively (<0.3), and intermediately (0.3–0.7) polarized

epicardium within the experimental field of view. As penetration depths are changed by 0.5–1.5 times their original values, the range of $V_{opt}$ normalized polarization decreases by 36% (1.36–0.87). Furthermore, $V_{opt}$ maps in Fig. 4 *C* show that areas of strong positive/negative polarization (>0.7 and <0.3) within the experimental field of view decrease, whereas areas of intermediate polarization (0.3–0.7) increase from 31.5% to 63.8%. Of particular interest in Fig. 4 *C* is the surface distribution of VEP on the LV for large penetration depths: as scattering volume increases (through increasing penetration depths), regions of strong negative polarization on the LV epicardium in the $V_{opt}$ maps align more directly above intramural excitable areas in the depth of the LV wall in the corresponding $V_m$ (SS = 11 V/cm/CI = 140 ms) map of Fig. 3. As penetration depths increase, fluorescent signals are sampled from greater depths. Thus, for large penetrations depths, the only regions of $V_{opt}$ on the epicardial surface which remain strongly negatively polarized (as seen close to the apex on the LV in Fig. 4 *C*) lie directly above intramural regions of tissue which have strong negative polarization throughout the depth of the ventricular wall (as seen in the corresponding transmural $V_m$ image in Fig. 3).

## Shock-induced arrhythmogenesis

For all chosen SS/CI here, postshock propagation evolves into arrhythmia generation. Figs. 5 and 8 present progression of this activity for the SS = 11 V/cm/CI = 140 ms episode; in this case sustained VT has a figure-of-eight pattern, with one rotor on the anterior and another on the posterior. The same type of arrhythmia is obtained in experiments, as illustrated by the activation map in Fig. 7 *A* (SS = 11 V/cm/CI = 140 ms), although here only the rotor on the anterior is visible in the experimental field of view.

We make a distinction here between immediate wavefront propagation after the shock (shock-induced arrhythmogenesis, defined as the period up to the completion of the first postshock beat) and sustained VT (analyzed in the following section), as the existence of residual VEP produces significantly different propagation and reentry patterns immediately after the shock than during sustained VT. For timings within the period of shock-induced arrhythmogenesis, epicardial and transmural $V_m$ distributions are presented in Fig. 5 *A*, top, and the bottom panel shows the corresponding epicardial $V_{opt}$ maps. The presence of residual VEP leads to complex wavefront propagation, often including entirely intramural wavefronts. Such propagation patterns are observed in the LV wall in $V_m$ maps of Fig. 5 *A*. In the first few milliseconds after the shock, the LV midmyocardium is largely refractory at the base, whereas tissue on and directly beneath the epicardium is negatively polarized (3 ms panels). The latter provides an excitable pathway and is traversed by a wavefront, which propagates on the epicardium from posterior to anterior (12 ms, 23 ms) but which cannot excite the refractory midmyocardium. Meanwhile, another wavefront is propagating into the intramural excitable area in the LV wall near the apex. At 39 ms, the two wavefronts coalesce and can now propagate into the LV midmyocardium, which has meanwhile recovered from the shock.

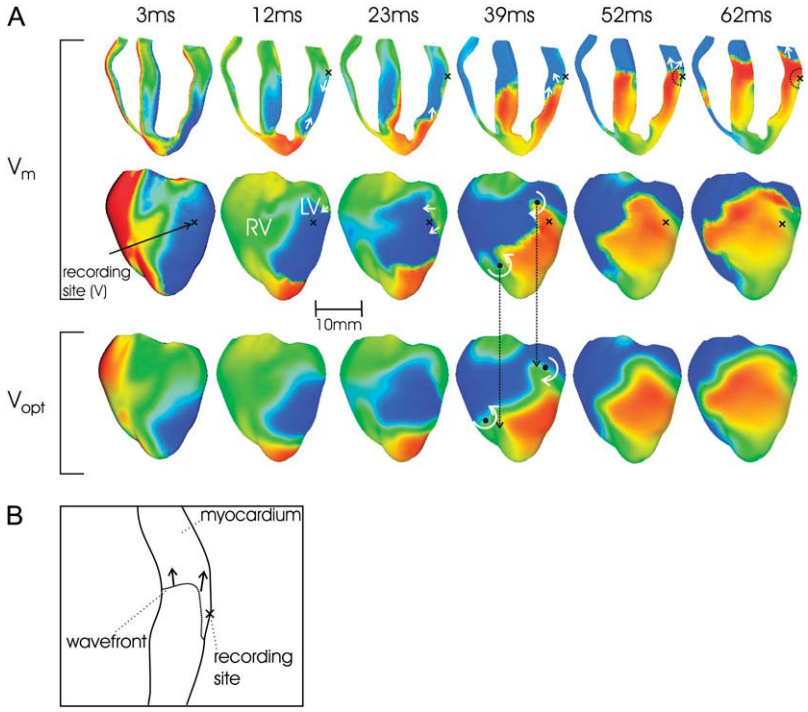


FIGURE 5 Shock-induced arrhythmogenesis. (*A*) Anterior epicardial $V_m$ and $V_{opt}$ distributions at several instances postshock for the SS = 11 V/cm/CI = 140 ms episode. Maps of $V_m$ in an apex-to-base cross section are also shown. White curved arrows in 39 ms maps indicate direction of spiral-wave rotation. Black dots represent phase singularities with long arrows indicating shifts in their locations. Straight white arrows depict directions of local propagation. Sites of dual-hump APs are marked by black crosses. Approximate scattering volume is shown by a dashed semicircle. (*B*) Schematic representation of subsurface wavefront propagation.

However, tissue on and directly beneath the epicardium is still depolarized from earlier excitation (23 ms) and thus activation only proceeds intramurally (52 ms). A schematic of this subsurface propagation is shown in Fig. 5 *B*. Similar entirely intramural wavefront propagation patterns were observed during other episodes of arrhythmia induction.

For the same episode of arrhythmogenesis as above, Fig. 6 shows the corresponding filaments (*purple*) at 54 ms, with $V_m$ distribution rendered semitransparent. Fig. 6 also presents the evolution of $V_m$ and $V_{opt}$ signals at specific epicardial locations. Similar experimental traces are depicted in Fig. 7, *B* and *C*, for the episode of shock-induced arrhythmogenesis illustrated in Fig. 7 *A*. Figs. 5 and 6 demonstrate that photon scattering results in significant differences between $V_m$ and $V_{opt}$ maps and traces during an episode of shock-induced arrhythmogenesis.

The underestimation of shock-end potentials shown in the previous section is clearly visible in the fluorescent traces. Traces in Fig. 6 also demonstrate that photon scattering results in prolonged AP upstroke and thus in increased width of the optical wavefront relative to $V_m$ (4,5) (evident in epicardial maps of Fig. 5). The increase in wavefront width, combined with photon scattering from a region of multilevel residual VEP surrounding a filament during shock-induced arrhthmogenesis, leads to shifts in the phase singularity locations on the epicardial surface in $V_{opt}$ as compared to $V_m$ maps, evident in the 39 ms panel of Fig. 5. This optical signal distortion is significant; for instance, the shift across the epicardial surface of the RV phase singularity location is 4.08 mm, which is larger than both core size and accuracy of the experimental phase singularity detection method (16).

The $V_{opt}$ trace v of Fig. 6 is from an epicardial site above the filament associated with the reentrant subsurface propagation described in Fig. 5 (location shown as *black cross*). The $V_{opt}$ trace has a noticeable second local maximum (hump) 20–30 ms after the initial peak of the AP, not present in the corresponding $V_m$ trace. In Fig. 5 *A*, the intramural wavefront propagates, to a large extent, within the scattering volume associated with the epicardial recording site (represented by *dashed black semicircle*), without breaking onto the epicardium. Photons emitted as the midmyocardium is depolarized by the intramural wave are scattered through the wall and detected in the recorded epicardial signal, appearing as a hump.

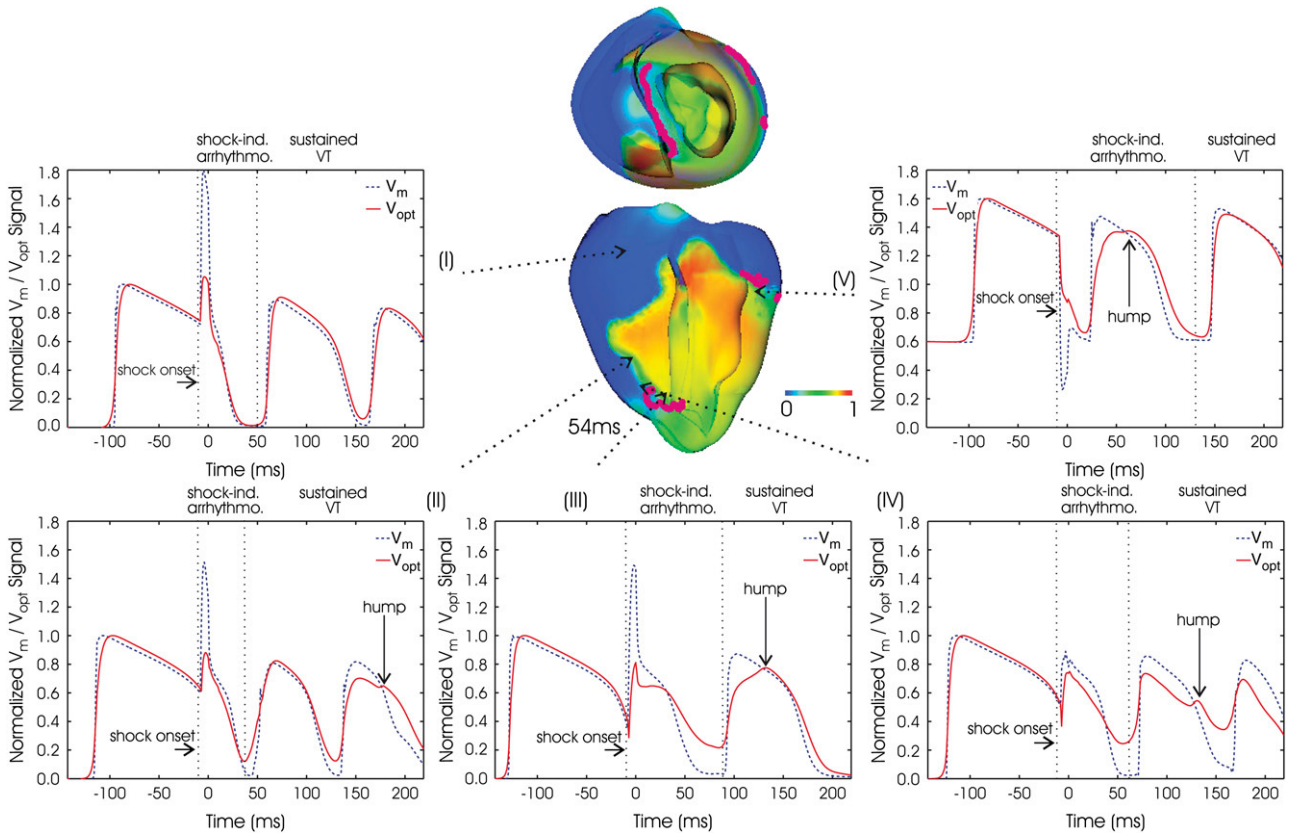


FIGURE 6 Time course of $V_m$ (*dashed blue lines*) and $V_{opt}$ (*solid red lines*) signals during periods of shock-induced arrhythmogenesis and sustained VT for the same episode as in Fig. 5. Semitransparent snapshots of $V_m$ distribution at 54 ms, with filaments in purple, indicate where signals are recorded from. Vertical dashed lines demarcate periods of shock-induced arrhythmogenesis and sustained VT.

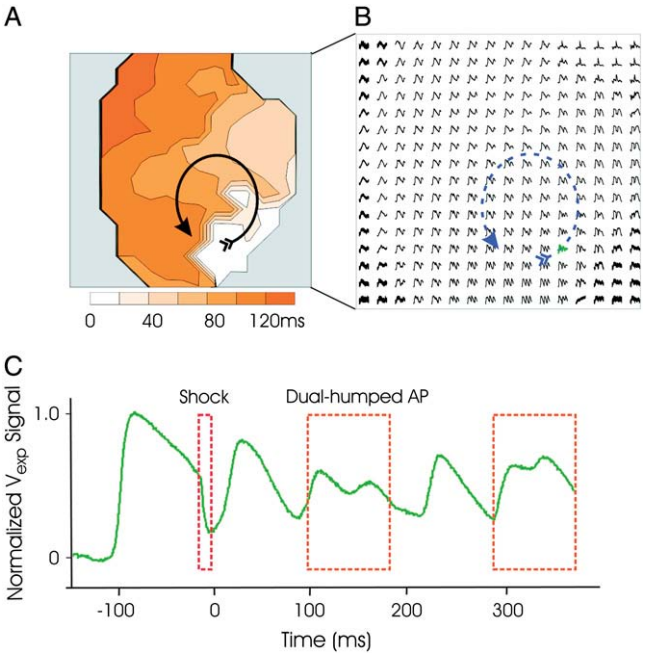


FIGURE 7 Experimental data on shock-induced reentry. (*A*) Anterior postshock optical activation map for the SS = 11 V/cm/CI = 140 ms episode. Arrow indicates reentrant pattern. (*B*) Optical AP traces. (*C*) Optical trace with dual-hump morphology from location near the core of reentry (shown in *green* in *B*).

## Sustained VT

During sustained VT, dual-hump APs are also recorded near surface phase singularities. Traces ii–iv of Fig. 6 show $V_m$ and $V_{opt}$ signals from epicardial sites above the filament; in these traces $V_{opt}$ signals exhibit the characteristic dual-hump morphologies. In contrast, a signal recorded far from the location of any filaments is shown in trace i; in this case $V_m$ and $V_{opt}$ track each other consistently after the shock throughout VT. Experimental dual-hump APs are also recorded from locations surrounding the core of the reentry on the epicardial surface, with regular APs recorded from locations farther from the core, portrayed in Fig. 7 *B*. A dual-dumped AP trace from Fig. 7 *B* is highlighted in Fig. 7 *C* (in *green*); it has morphologies similar to the simulated traces ii–v in Fig. 6.

Experimental and simulated optical traces also demonstrate that for recordings close to a phase singularity, the minimum potential that precedes the next AP is elevated and the AP magnitude is diminished with respect to their values during pacing. These features are not observed in $V_m$ traces, nor traces recorded far from the core of reentrant activity, and are particularly apparent in traces with dual-hump morphologies.

In sustained VT, we also observe dual-hump APs due to subsurface propagation, as in shock-induced arrhythmogenesis; however, this mechanism is less frequent (not present in the episode depicted in Fig. 6). However, Fig. 6, traces ii and iv, indicates that other scattering mechanisms also lead to dual-hump morphologies, illustrated in Fig. 8 and elucidated below.

### *Delayed propagation in the septum*

In Fig. 8 *A* (63 ms, 87 ms), a wavefront propagates from apex to base through the septum and LV wall, leaving the apical septum refractory. Meanwhile, a second wavefront propagates downward through the RV, depolarizing the recording site (*black cross*) at ~70 ms. When this second wavefront reaches the apex, tissue there has recovered, allowing propagation into the excitable area in the apical LV wall. However, it cannot propagate into the septum, as tissue there is still refractory (87 ms). A few milliseconds later, septal tissue recovers, and the wave can propagate into the excitable area left behind, doing so asymmetrically (107 ms). Finally, the wave propagates up the RV side of the septum (124 ms, 135 ms), emitting photons which scatter through the thin RV in the highlighted region as the tissue depolarizes; these are recorded as a second hump, with a delay from the initial depolarization of the recording site. After this dual-hump morphology, resting potential is elevated because although the recording site is at rest, tissue in the septum (which constitutes a large percentage of the scattering volume) is still refractory. The 124 ms panels in Fig. 8 show that when residual VEP is no longer present, the difference in phase singularity locations between $V_m$ and $V_{opt}$ maps is 1.15 mm, significantly less than during shock-induced arrhythmogenesis.

### *Surface wavefront collision*

In Fig. 8 *B*, the dual-hump morphology of trace ii of Fig. 6 is predominantly due to lateral scattering in a direction parallel to the epicardium. There is a complex propagation on the epicardium (132 ms, 152 ms), with a wavefront propagating upward and across the LV, rotating about the filament shown in Fig. 6. This causes the recording site (*black cross*) to depolarize after 140 ms. In the 165 and 175 ms panels, a second wavefront propagates around the RV toward the recording site. However, the 175 ms panel shows that this wavefront collides with the first wavefront. As tissue in the vicinity of the recording site is depolarized by the second wavefront, the emitted photons are scattered laterally, parallel to the epicardium, and are detected as a hump 40 ms after the initial depolarization.

Since these unusual AP characteristics arise because information regarding transmembrane potentials within a volume is transduced via photon scattering, we hypothesize that dual-hump morphologies depend on scattering volume dimensions. Fig. 9 demonstrates how varying the penetration depths for illumination and emission alters the $V_{opt}$ trace at site iv of Fig. 6. Panel *A* in Fig. 9 shows that increasing penetration depth, and thus scattering volume, leads to i), elevation of

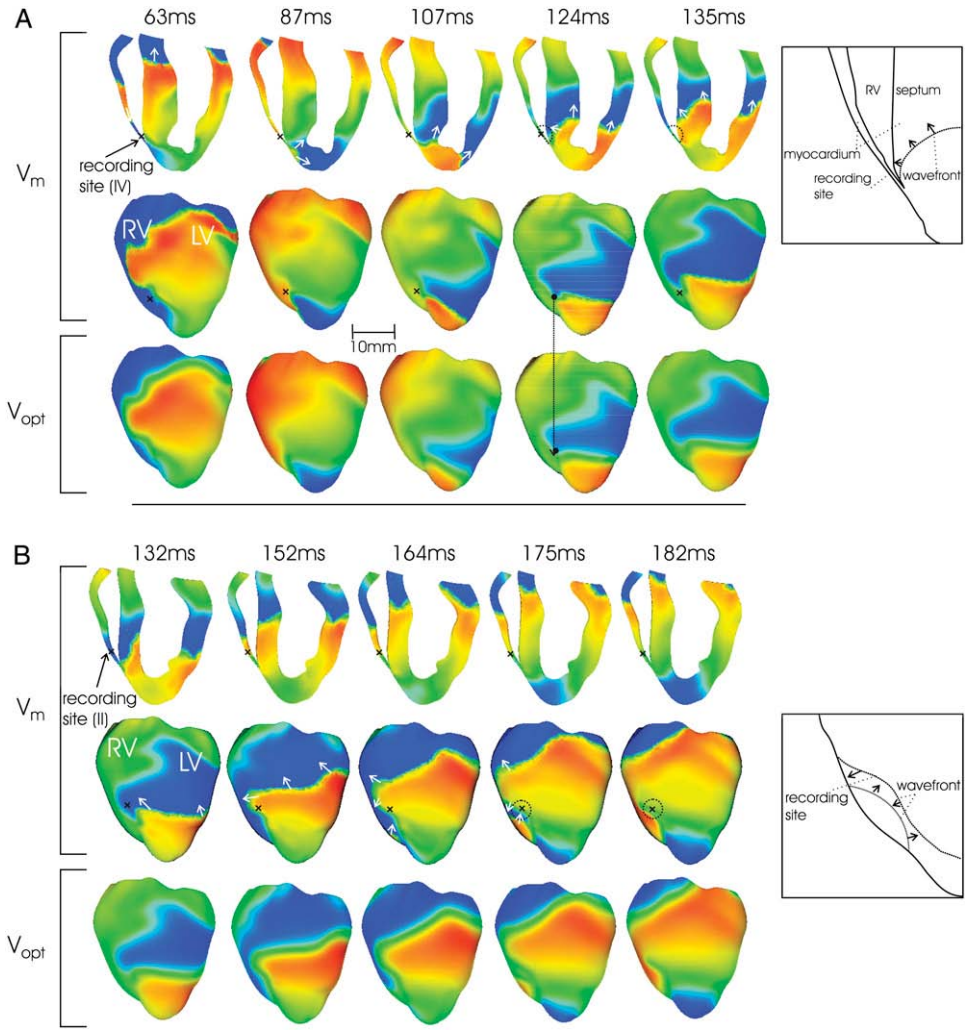


FIGURE 8 Simulated $V_m$ (anterior epicardial and in a cross section) and $V_{opt}$ maps during sustained VT; notations are as in Fig. 5. Schematic drawings (*right*) present formation of dual-hump APs due to *A*, delayed propagation into septum (Fig. 5, *trace iv*); and *B*, surface wavefront collision (Fig. 6, *trace ii*).

diastolic potential, ii), decrease in AP amplitude, and iii), increase in the amplitude of the hump. The dual-hump ratio, defined as the ratio of the amplitude of the hump to that of the initial AP depolarization, is depicted in Fig. 9 *B*.

Changes in dual-hump ratio and resting potential with increases in penetration depth are quantified in Fig. 9, *C* and *D*. Our results demonstrate that increasing penetration depths from 0.5 to 1.5 times their default values results in an increase in normalized resting potential from 0.09 to 0.36, along with an increase in dual-hump ratio from 0.63 to 0.82.

## DISCUSSION

The goal of this study was to provide a comprehensive understanding of the role of 3D fluorescent photon scattering in signal distortion during optical mapping of arrhythmias and defibrillation. The anatomically realistic bidomain model of the rabbit ventricles was combined with an accurate representation of 3D photon scattering in the ventricles to develop a unique model of panoramic optical imaging. This approach allowed us to simulate transmembrane potential distributions during arrhythmia and defibrillation and compare them to the corresponding simulated optical maps, revealing distortion mechanisms specific to each electrophysiological scenario (sustained VT, shock-induced arrhythmogenesis, or VEP). The simulation approach was complemented by experiments on intact rabbit hearts, the results of which served both as model input (optical parameters of the tissue) and as means of model validation.

For the first time, our simulations reveal the mechanisms by which photon scattering can give rise to optical signal characteristics such as dual-hump morphologies, elevated resting potentials, and reduced AP amplitudes near the reentrant core, as well as to shifts in the phase singularity locations. During the defibrillation strength shock, scattering significantly modulates the magnitude of the optically recorded VEP. The close match between simulated and experimental optical maps demonstrates that these specific mechanisms of distortion, stemming from photon scattering, are intrinsic to the fluorescent imaging

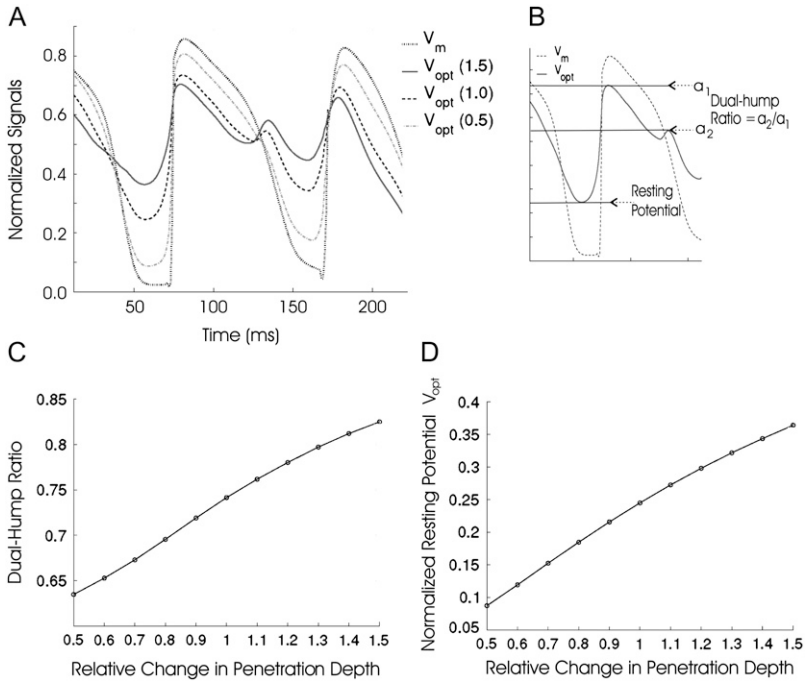


FIGURE 9 (*A*) $V_{opt}$ dual-hump AP from Fig. 6, trace iv, together with the same signals obtained upon variations of penetration depths at illumination and emission wavelengths by 0.5, 1.0, and 1.5 times their default values. The corresponding $V_m$ trace is also shown. (*C* and *D*) Changes in resting potential and dual-hump ratio for variations in penetration depths as in *A*. Panel *B* shows how quantities in *C* and *D* are measured.

technique. Each of these mechanisms is discussed in the sections below.

This study, together with our previous publication on optical signal distortion during pacing (5), clearly demonstrates the necessity to 1), accurately model scattering of photons in all directions (i.e., 3D) and not only in the direction normal to the tissue surface (i.e., one-dimensional (1D)), as assumed previously (3,6), thus allowing the effects of scattering in the plane parallel to the epicardium to be also evaluated; and 2), represent realistically ventricular anatomy, as opposed to assuming idealized tissue geometries (3,4,6), thus allowing the detection of distortions associated with propagation of complex wavefronts. Both features place our optical imaging model in a unique position to provide accurate assessment of distortion mechanisms arising from photon scattering.

## Modulation of shock-end VEP

In agreement with previous studies (11), our simulations demonstrate that at the end of a strong shock, a complex VEP is induced throughout the ventricles, with the epicardium strongly polarized and polarization magnitude dramatically diminishing (or even changing sign) in the depth of the wall. Optical mapping experiments after identical shock protocols have found, however, significantly weaker shock-end VEP on the epicardium (9,11). We demonstrate that 3D photon scattering accounts for this discrepancy. Indeed, because VEP of diminishing magnitude is distributed, at the time of shock termination, within a scattering volume beneath an epicardial recording site, the optical signal at that instant, which represents a ''weighted-average'' of VEP values within that volume, has a lower resultant value as compared to the VEP value at the actual epicardial site.

As a result of this averaging effect, the overall degree of optical signal distortion at shock-end depends upon the specific distribution of transmural VEP beneath the epicardial surface. Specifically, it depends upon the difference between the magnitude of the epicardial VEP at the recording site and VEP magnitude in midmyocardial tissue residing just beneath that site (2). Polarization residing below this depth contributes only very weakly to the signal. Therefore, differences in ventricular wall thicknesses at different ventricular locations and between RV and LV have only a minor role in optical signal distortion by photon scattering.

Our results demonstrate not only that the gap between simulated and optically recorded VEP is bridged by accounting for 3D photon scattering but also that it is also possible to use the optical maps to obtain information about the distribution of excitable areas created by the shock (areas of VEP around or below rest) in the depth of the myocardial wall. These areas provide an avenue for postshock propagation, often before the surfaces recover from the shock. Therefore, knowledge of their location and extent could be critical in devising strategies to halt postshock propagation and alter shock outcome. As shown in Fig. 4 *C*, if photon scattering is maximized (by appropriate preparations and fluorescent dyes (17)), then regions of strong epicardial negative polarization in optical maps lie directly above intramural excitable areas.

### Shift in phase singularity locations

In arrhythmia research, locating phase singularities is a widely used analysis tool (16,18). We demonstrate that photon scattering is manifested as a shift in the phase singularity locations obtained by processing the optical maps. Since phase singularities/scroll-wave filaments are surrounded by different levels of transmembrane potential, the distribution of transmembrane potential within a scattering volume associated with a recording site near the reentrant core is highly heterogeneous, resulting in signal distortion as these differences are transduced through the myocardial wall by scattered photons. As a filament is an intrinsic 3D entity, assessing correctly the magnitude of this distortion depends critically upon the inclusion of 3D photon scattering in the model. If photon scattering were assumed to occur only in depth (1D, i.e., in the direction normal to the surface), then a shift in the phase singularity location would occur only if the filament is at an angle to the surface. This is because for a filament orientated normally to the epicardium, potential values do not differ along the normal; thus the results of 1D depth averaging would predict no shift. However, accounting for photon scattering within a volume (3D) results in a shift, due to differences in potential levels within this volume. This shift is amplified by arbitrary filament orientations and particularly by filament bending below the epicardium, as variations in transmembrane potential then occur closer to the surface, where fluorescence is stronger. Thus, accounting for 3D rather than 1D scattering and complex filament orientations explains the significantly larger shifts documented here, as compared to shifts of just $0.57 \pm 0.16$ mm found in Bray and Wikswo (3). The shift in the positions of optically recorded phase singularities, as found here, could have important implications for the application of localized stimuli near the epicardial spiral-wave core and the ability to control spiral-wave dynamics (19).

### Dual-hump APs

This study demonstrates that 3D scattering in regions near the scroll-wave filament is manifested in the optically recorded APs as dual-hump morphologies. Previous studies have attributed such morphologies exclusively to subsurface wavefronts passing close to, but not breaking onto, the epicardial surface (3,8). Here we uncovered two additional mechanisms for dual-hump AP formation: 1), wavefront collision on the epicardium, with dual-hump morphology arising from photon scattering in a plane parallel to the epicardium as well as from depth; and 2), delayed propagation into the septum, with dual-hump morphology stemming from fluorescent photons scattering through the RV cavity. A phenomenon similar to the latter has been documented in optical recordings of rabbit papillary muscles, whereby dual-hump APs were eliminated by placing opaque plastic over the septum, thus shielding scattered fluorescent photons carrying an electrophysiological signature of the septum (20). These findings provide insight into the contribution of 3D fluorescent photon scattering to the generation of dual-humped APs in experimental optical recordings and the role played by intramural wavefront propagation and ventricular anatomy made possible through the realistic ventricular model used in the study.

### Resting potential elevation/decrease in AP amplitude

Our results demonstrate that elevation of resting potential and decrease in the amplitude of fluorescent APs, relative to the corresponding levels during pacing, recorded near scroll-wave filaments can be solely attributable to 3D photon scattering. Specifically, these effects are due to a combination of the heterogeneous distribution of transmembrane potentials near the filament and the normalization procedure used in optical mapping experiments. Optical APs at a given site are normalized by the amplitude of the paced optical AP at that site. However, such normalization limits are specific to wavefront propagation through the scattering volume beneath the particular recording site. During pacing, optical mapping records a maximum value of the AP when the entire scattering volume associated with the recording site is depolarized; depending on conduction velocity and scattering volume dimensions, this occurs a few milliseconds after the single pacing-induced wavefront passes by the recording site. Similarly, optical resting potential is measured before the wavefront arrives at the recording site and corresponds to the entire scattering volume being at rest.

During arrhythmia, however, propagation through the scattering volume associated with a recording site near the filament is more complex than during pacing; the entire scattering volume is never depolarized or at the resting potential at the same time, i.e., when the recording site itself is depolarized (or at rest), typically not all the tissue within the scattering volume is depolarized (or at rest). The normalization limits obtained from pacing subsequently under-/overestimate the local maximum/minimum of the optical AP at the recording site. Although changes in diastolic potential and AP amplitude close to the core of reentry during arrhythmia have been shown to be attributed to ion accumulation, this typically takes a number of reentrant cycles to develop. The findings from our study demonstrate that such changes, observed in this case in the stages of reentry formation, can be solely explained by optical signal distortion due to fluorescent photon scattering.

### Variation in optical parameters

Photon scattering/absorption parameters and the corresponding optical penetration depths vary widely, depending on a large number of factors including the fluorescent dye used, the wavelength of recording, the specifics of the tissue preparations (i.e., blood or Tyrode's perfused), and variations

between species. Even for animals of the same species, there can be large variability in the optical properties of the preparation (2), due to factors such as age and degree of heterogeneity within the tissue (fibroblast and fatty tissue density). In addition, accurate experimental measurement of the optical parameters in a given preparation is subject to limitations (discussed below). Therefore throughout this study, simulations were performed with optical penetration depths ±50% of their measured values to account for this difference. More importantly, however, these variations act to further underscore the large role played by photon scattering in optical signal distortion. From the figures showing the effects of optical parameter variation (Figs. 3 and 8), it is evident that for small penetration depths $V_{opt}$ tends toward $V_m$, whereas as penetration depths increase, all of the observed effects, such as modulation of shock-end VEP, dual-humped AP morphology, and increase in AP resting potential/decrease in AP amplitude, are all significantly accentuated.

### Study limitations

The limitations of the rabbit ventricular bidomain model and experimental techniques have been outlined elsewhere (11). Limitations of the optical model include i), effects of lens and optics of the detection system not being represented (thought to be secondary to photon-scattering distortion analyzed here); ii), the lack of small-scale tissue heterogeneities in the model and the impact these might have on light scattering/absorption in localized regions; and iii), the use of the excitation contraction uncoupling agent BDM not completely removing motion artifacts, although these small remaining distortions are not thought to affect the findings in this study.

Our method to experimentally measure optical penetration depths at the illumination and emission wavelengths, although employed in previous studies (1,4), is also subject to limitations. The technique infers photon density in the depth of the tissue by recording photon intensity exiting perpendicularly from the cut tissue surface. Although approximate, this technique has been shown to provide an accurate assessment of optical penetration depths in myocardium (1,4). Moreover, the measured values of optical penetration depths obtained here agree closely with those determined in previous studies (1,2,4). Nonetheless, to accommodate uncertainty in the experimentally measured values of the penetration depths as well as possible variations in optical parameters between individual tissue samples throughout this study, values of the optical penetration depths were varied and an assessment of the effect of this variation on the simulated optical signal was conducted.

The quantitative analysis performed in this study (particularly regarding the shock-end VEP distributions where percentages of surface areas with different polarization levels were compared for $V_m$, $V_{opt}$, and $V_{exp}$) was specific to the experimental system used here where the field of view encompasses parts of RV and LV. However, this was used only as a quantitative validation of the optical model. The major findings in this study, including distortion of optically recorded shock-end VEP due to transduction of information from weakly polarized midmyocardial regions by fluorescent photon scattering and the optical artifacts in the fluorescent signals during shock-induced arrhythmogenesis and VT, are common to all experimental systems, as they are inherent consequences of the optical mapping technique itself.

Despite its limitations, this study demonstrates an excellent match between simulations and experiments and presents a compelling set of mechanisms for photon-scattering-induced distortion in optical signals.

This work was supported by the United Kingdom Engineering and Physical Sciences Research Council through a Life Sciences Interface Doctoral Training Centre studentship (GR/S58119/ 01, M.J.B.) and Integrative Biology E-Science pilot project (GR/S72023/01, D.J.G.), the United Kingdom National Grid Service, and a National Science Foundation (CBET-0601935, N.A.T.) and National Institutes of Health award (HL063195, HL082729, N.A.T., and HL074283, I.R.E).

## REFERENCES

1. Baxter, W. T., S. F. Mironov, A. V. Zaitsev, J. Jalife, and A. M. Pertsoz. 2001. Visualizing excitation waves inside cardiac muscle using transillumination. *Biophys. J.* 80:516–530.
2. Ding, L., R. Splinter, and S. Knisley. 2001. Quantifying spatial localization of optical mapping using Monte Carlo simulations. *IEEE Trans. Biomed. Eng.* 48:1098–1107.
3. Bray, M. A., and J. P. Wikswo. 2003. Examination of optical depth effects on fluorescence imaging of cardiac propagation. *Biophys. J.* 85: 4134–4145.
4. Hyatt, C. J., S. F. Mironov, M. Wellner, O. Berenfeld, A. K. Popp, D. A. Weitz, J. Jalife, and A. M. Pertsov. 2003. Synthesis of voltage-sensitive fluorescence signals from three-dimensional myocardial activation patterns. *Biophys. J.* 85:2673–2683.
5. Bishop, M. J., B. Rodriguez, J. Eason, J. P. Whiteley, N. A. Trayanova, and D. J. Gavaghan. 2006. Synthesis of voltage-sensitive optical signals: application to panoramic optical mapping. *Biophys. J.* 90:2938–2945.
6. Janks, D. L., and B. J. Roth. 2002. Averaging over depth during optical mapping of unipolar simulation. *IEEE Trans. Biomed. Eng.* 49:1051–1054.
7. Girouard, S. D., K. R. Laurita, and D. S. Rosenbaum. 1996. Unique properties of cardiac action potentials with voltage-sensitive dyes. *J. Cardiovasc. Electrophysiol.* 7:1024–1038.
8. Efimov, I. R., V. Sidorov, Y. Cheng, and B. Wollenzier. 1999. Evidence of three-dimensional scroll waves with ribbon-shaped filaments as a mechanism of ventricular tachycardia in isolated rabbit heart. *J. Cardiovasc. Electrophysiol.* 10:1451–1462.
9. Efimov, I. R., F. Aguel, Y. Cheng, B. Wollebzier, and N. A. Trayanova. 2000. Virtual electrode polarization in the far field: implications for external defibrilation. *Am. J. Physiol. Heart Circ. Physiol.* 279:H1055–H1070.
10. Kleber, A. G., and Y. Rudy. 2004. Basic mechanisms of cardiac impulse propagation and associated arrhythmias. *Physiol. Rev.* 84:431–488.
11. Rodriguez, B., L. Li, J. C. Eason, I. R. Efimov, and N. A. Trayanova. 2005. Differences between left and right ventricular chamber geometry affect cardiac vulnerability to electric shocks. *Circ. Res.* 97:168–175.
12. Roth, B. R. 2002. Artifacts, assumptions, and ambiguity: pitfalls in comparing experimental results to numerical simulations when studying electrical stimulation of the heart. *Chaos.* 12:973–981.

13. Trayanova, N. A., J. Eason, and F. Aguel. 2002. Cardiac defibrillation: a look inside the heart. *Comput. Vis. Sci.* 4:259–270.

14. Ashihara, T., and N. A. Trayanova. 2004. Asymmetry in membrane responses to electric shocks: insights from bidomain simulations. *Biophys. J.* 87:2271–2282.

15. Larson, C., L. Dragnev, and N. A. Trayanova. 2003. Analysis of electrically induced reentrant circuits in a sheet of myocardium. *Ann. Biomed. Eng.* 31:768–780.

16. Iyer, A. N., and R. A. Gray. 2001. An experimentalist's approach to accurate localization of phase singularities during reentry. *Ann. Biomed. Eng.* 29:47–59.

17. Cheong, W. F., S. A. Prahl, and A. J. Welch. 1990. A review of the optical properties of biological tissues. *IEEE J. Quantum Electron.* 26:2166–2175.

18. Jalife, J., R. A. Gray, G. E. Morely, and J. M. Davidenko. 1998. Self-organization and the dynamical nature of ventricular fibrillation. *Chaos.* 8:79–93.

19. Ashihara, T., T. Namba, M. Ito, T. Ikeda, K. Nakazawa, and N. A. Trayanova. 2004. Spiral wave control by a localized stimulus: a bidomain model study. *J. Cardiovasc. Electrophysiol.* 15:226–233.

20. Al-Khadra, A., V. Nikolski, and I. R. Efimov. 2000. The role of electroporation in defibrillation. *Circ. Res.* 87:797–804.